

# Fast retrieval of XCO<sub>2</sub> over East Asia based on the OCO-2 spectral measurements

Fengxin Xie<sup>1,a</sup>, Tao Ren<sup>1</sup>, Changying Zhao<sup>1</sup>, Yuan Wen<sup>2</sup>, Yilei Gu<sup>2</sup>, Minqiang Zhou<sup>3</sup>, Pucai Wang<sup>3</sup>, Kei Shiomi<sup>4</sup>, and Isamu Morino<sup>5</sup>

<sup>1</sup>China-UK Low Carbon College, Shanghai Jiao Tong University, Shanghai, China

<sup>2</sup>Shanghai Institute of Satellite Engineering, Shanghai, China

<sup>3</sup>Institute of Atmospheric Physics, Chinese Academy of Science, Beijing, China

<sup>4</sup>Earth Observation Research Center, Japan Aerospace Exploration Agency, 2-1-1 Sengen, Tsukuba, Ibaraki 305-8505, Japan

<sup>5</sup>Satellite Remote Sensing Section and Satellite Observation Center, Earth system Division, National Institute for Environmental Studies, Onogawa 16-2, Tsukuba, Ibaraki 305-8506, Japan

<sup>a</sup>Currently at: Atmosphere and Ocean Research Institute, the University of Tokyo, Chiba, Japan

**Correspondence:** Tao Ren (tao.ren@sjtu.edu.cn)

**Abstract.** The increase in greenhouse gas concentrations, particularly CO<sub>2</sub>, has significant implications for global climate patterns and various aspects of human life. Spaceborne remote sensing satellites play a crucial role in high-resolution monitoring of atmospheric CO<sub>2</sub>. However, the next generation of greenhouse gas monitoring satellites is expected to face challenges, particularly in terms of computational efficiency in atmospheric CO<sub>2</sub> retrieving and analysis. To address these challenges, this study focuses on improving the speed of retrieving the column-averaged dry air mole fraction of carbon dioxide (XCO<sub>2</sub>) using spectral data from the OCO-2 satellite, while still maintaining retrieval accuracy. A novel approach based on neural network (NN) models is proposed to tackle the nonlinear inversion problems associated with XCO<sub>2</sub> retrievals. The study employs a data-driven supervised learning method and explores two distinct training strategies. Firstly, training is conducted using experimental data obtained from the inversion of the operational optimization model, which is released as the OCO-2 satellite products. Secondly, training is performed using a simulated dataset generated by an accurate forward calculation model. The inversion and prediction performance of the machine learning model for XCO<sub>2</sub> are compared, analyzed, and discussed for the observed region over East Asia. The results demonstrate that the model trained on simulated data accurately predicts XCO<sub>2</sub> in the target area. Furthermore, when compared to OCO-2 satellite product data, the developed XCO<sub>2</sub> retrieval model not only achieves rapid predictions (<1 ms) with good accuracy (1.8 ppm or approximately 0.45%), but also effectively captures sudden increases of XCO<sub>2</sub> plumes near industrial emission sources. The accuracy of the machine learning model's retrieval results is validated against reliable data from TCCON sites, demonstrating its capability to capture CO<sub>2</sub> seasonal variations and annual growth trends effectively.

## 1 Introduction

Since the Industrial Revolution, human activities have released large amounts of greenhouse gases, primarily carbon dioxide, into the atmosphere. This continual increase in emissions has led to global warming and disrupted human societies and ecosys-

tems (Zehr, 2015). Accurately estimating atmospheric carbon fluxes is critical for implementing effective emission reduction strategies at national and regional levels. However, precise carbon flux estimates require assimilating carbon dioxide concentration data across regions, using measurements of atmospheric column-averaged dry air mole fraction of carbon dioxide ( $XCO_2$ ) (Jin et al., 2021). Direct measurement methods like balloons or aircraft have challenges in obtaining global-scale data.

25 Currently, the main monitoring approach uses spectrometers to record spectra in  $CO_2$  absorption bands, followed by inversion algorithms to derive  $XCO_2$ . The two primary monitoring methods are ground-based monitoring stations and satellite remote sensing.

The Total Carbon Column Observing Network (TCCON) provides ground-based monitoring of atmospheric carbon dioxide through a global network of high-precision Fourier transform spectrometers (Wunch et al., 2011, 2015). However, TCCON sites

30 are sparsely distributed and cannot be deployed in regions with unfavorable geography or harsh climates. Consequently, the network lacks the extensive spatial coverage required for comprehensive global carbon monitoring and carbon cycle analysis. Nevertheless, the ultra-high spectral resolution of TCCON spectrometers enables highly accurate retrievals of  $XCO_2$ . Under clear sky conditions, TCCON precision can reach 0.1% (<0.4 ppm). Under relatively clear conditions with minimal clouds and aerosols, precision remains within 0.25% (<1 ppm) (Messerschmidt et al., 2011). Due to such high precision and accuracy,

35 TCCON data are invaluable for validating satellite-based  $XCO_2$  products (Cogan et al., 2012; Wunch et al., 2017; Liang et al., 2017) and comparing them to carbon cycle models. However, the spatial limitations of the network underscore the need for satellite remote sensing to provide regular global measurements of atmospheric carbon dioxide.

High-spectral-resolution greenhouse gas monitoring satellites employ spectrometers on orbit to measure solar radiation spectra after interaction with the Earth's atmosphere and ground surface (Meng et al., 2022). Unlike ground monitoring, satellite remote sensing offers broader spatial coverage and more flexible temporal observation globally. Consequently, satellite remote sensing has become vital for greenhouse gas monitoring worldwide. Notable ongoing passive  $CO_2$  observation missions include China's TanSat (Liu et al., 2018), Japan's GOSAT (2009) and GOSAT-2 (2018) (Hamazaki et al., 2005; Kuze et al., 2009; Imasu et al., 2023), and the United States' OCO-2 (2014) and OCO-3 (2018) (Crisp et al., 2017; Eldering et al., 2019). Upcoming missions are France's MicroCarb by CNES (Cansot et al., 2023), ESA's  $CO_2M$  (Sierk et al., 2021) and

45 GOSAT-GW (Matsunaga and Tanimoto, 2022). The next-generation greenhouse gases monitoring satellites mainly address the challenge of improving the spatial and temporal resolutions of observations. However, single satellites still have resolution, coverage, and meteorological limitations for regional emission monitoring. Enhancing satellite sensor performance alone cannot produce datasets sufficient for monitoring carbon sources and sinks. Improving the accuracy and efficiency of satellite data inversion is also crucial. Integrating data from multiple satellites into a coordinated system is necessary to fully capture

50 dynamic changes in regional carbon sources and sinks. Developing new high-precision, high-throughput inversion methods to efficiently derive accurate greenhouse gas concentration distributions from satellite data is a key challenge needing attention.

The mainstream inversion algorithms (O'Dell et al., 2012; Crisp et al., 2012; Yoshida et al., 2013) for retrieving greenhouse gas concentrations from high-spectral-resolution satellite measurements are based on nonlinear Bayesian optimization theory (Rodgers, 2000) and full physics models. In essence, these algorithms operate by iteratively adjusting estimated gas concentration profiles and other atmospheric and surface parameters in a radiative forward model to minimize the mismatch

55

between simulated and observed spectra. More specifically, the inversion process starts with an initial atmospheric state guess, including trace gas concentration profiles as functions of pressure/altitude. Radiative transfer equations are then solved to simulate the top-of-atmosphere radiance spectrum observed by the satellite for this atmospheric state. The simulated spectrum is compared to the actual observed spectrum, calculating the difference, covariance and cost function. The input gas profiles and model parameters are iteratively adjusted to reduce the cost function over multiple rounds of radiative transfer simulations. Once simulated spectra closely match observations, the model state is output as the retrieved concentration profile. However, executing these complex optimizations requires computationally expensive interpolation of high-spectral-resolution gas absorption reference data and solving the radiative transfer equations in each iteration. Running the radiative forward model repeatedly for every adjusted atmospheric state also leads to slow overall inversion. Consequently, optimization-based retrievals struggle to match increasing satellite observation volumes and throughput needs. This inherent inefficiency has become a major obstacle to operational greenhouse gas monitoring using current and planned high-resolution spectrometers. While rigorous, standard nonlinear optimization retrievals lack the speed and scalability required for high-precision real-time or near-real-time greenhouse gas mapping satellite-based greenhouse gas mapping. Overcoming this bottleneck necessitates new inversion approaches that can ingest high-resolution spectral data and retrieve concentrations with both accuracy and computational efficiency.

In recent years, machine learning has demonstrated exceptional performance across various research fields, with the discovery of potential nonlinear relationships between data as one of its fundamental and crucial applications. Regarding the important applications of carbon dioxide (CO<sub>2</sub>) retrieving, Carvalho et al. (2010) attempted to retrieve the vertical CO<sub>2</sub> profiles using spectral data from SCIAMACHY's 6 channels (1000-1700 nm). The overall precision and bias of the retrieved results were estimated to be approximately 1.0% and less than 3.0%, respectively. Gribanov et al. (2010) developed a two-hidden-layer multilayer perceptron (MLP) model to retrieve CO<sub>2</sub> vertical concentrations by reflected solar radiation measured by the GOSAT TANSO-FTS sensor, achieving an inversion accuracy better than 1 ppm for CO<sub>2</sub> column-averaged values and better than 4 ppm for surface CO<sub>2</sub> concentrations for the test samples. In the study conducted by Zhao et al. (2022), a two-step machine learning approach was developed for retrieving atmospheric XCO<sub>2</sub> using spectral data from the GOSAT weak-CO<sub>2</sub> band. They established a direct one-dimensional line-by-line forward model to simulate GOSAT's observed spectra within the 6180-6280 cm<sup>-1</sup> spectral interval, forming the foundation for training their machine learning model. The retrieval model operates by initially obtaining the atmospheric spectral optical thickness, followed by extracting XCO<sub>2</sub> from this optical thickness spectra. As a proof-of-concept, the method was tested in Australia under clear sky conditions using GOSAT's spectra, demonstrating an accuracy of approximately 3 ppm for XCO<sub>2</sub> retrieval. The study also discussed potential enhancements to further refine the accuracy of this retrieval method. Keely et al. (2023) employed the machine learning method of Extreme Gradient Boosting (Chen and Guestrin, 2016) to develop a nonlinear bias correction approach for OCO-2 version 10 product, significantly reducing systematic errors in CO<sub>2</sub> measurements and improving data quality, with an increase in sounding throughput by 14%. David et al. (2021) and Bréon et al. (2022) attempted to establish correlations between XCO<sub>2</sub> in the European Centre for Medium-Range Weather Forecasts' CAMS (Copernicus Atmosphere Monitoring Service) database and OCO-2 satellite monitoring spectra using multilayer perceptron artificial neural network models. However, their recent research (Bacour et al.,

2023) indicates that when the test dataset extends beyond the time range covered by the training dataset, the predicted results show a slight bias, approximately 2.5 ppm per year. Practical deployment of machine learning techniques for remote sensing demands additional research into the generalization performance of models on new observational data distributions beyond those encountered during training.

95 In the present paper, a proof-of-concept study demonstrates a novel machine learning strategy to accurately and efficiently retrieve atmospheric XCO<sub>2</sub> value from OCO-2 satellite spectral measurements. The model rapidly retrieves XCO<sub>2</sub> directly from OCO-2 spectral data, eliminating the need for repetitive radiative transfer simulations required by traditional nonlinear optimization retrieval algorithms. Additionally, the model enables the prediction of future XCO<sub>2</sub> values. The method was validated by comparing the retrieved XCO<sub>2</sub> against OCO-2 satellite version-10r products and ground-based TCCON measurements, confirming the accuracy of our efficient spectral inversion approach. The model also successfully demonstrated its  
100 capability to detect local plume features, indicating its potential utility in monitoring and analyzing specific emission sources. A major innovation in the present study is using accurate radiative transfer simulations to generate the training data, rather than relying solely on experimental data products. This simulation-based training approach could help overcome limitations in existing experimental data. Additionally, our neural network model achieves XCO<sub>2</sub> retrieval speeds orders of magnitude  
105 faster than traditional methods, reducing computation time from multiple seconds to less than 1 millisecond. This dramatic improvement in retrieval efficiency could enable real-time processing of the massive data volumes expected from next-generation greenhouse gas monitoring satellites. Importantly, our model achieves a precision of **less than 1.8 ppm**, competitive with the current state-of-the-art in retrieval accuracy. We also demonstrate the ability to accurately capture temporal variations and trends in XCO<sub>2</sub> by validating against reliable TCCON ground-based data. This level of verifiable performance is an important  
110 capability. This provides an effective solution for rapid inversion of large-scale, high-spectral-resolution remote sensing data in the future.

## 2 The machine learning based XCO<sub>2</sub> retrieval model

### 2.1 Targeted area and data screening

This proof-of-concept study aims to develop and validate an accurate and efficient machine learning-based XCO<sub>2</sub> retrieval  
115 model applied to the long OCO-2 time series for the East Asian region. Currently, similar global XCO<sub>2</sub> retrieval models rely on computationally intensive physical models. Our goal is to demonstrate a more efficient data-driven approach using MLP neural networks.

Before developing the machine learning based fast retrieval model, we implemented several preprocessing steps on the OCO-2 observational dataset (OCO-2 Science Team et al., 2020a) for the target East Asian area spanning between 20°N-  
120 45°N and 110°E-145°E, as shown in Fig. 1. Specifically, we filtered the data both spatially and temporally to focus only on observations within this geographic region and time period of interest (2016-2021). Additionally, we filtered the data to only include Nadir mode observations marked as “Good” based on the quality flag indicator (“xco2\_quality\_flag” = 0 in OCO-2 Lite v10r files (OCO-2 Science Team et al., 2020b)), as these represent the highest quality OCO-2 measurements.

Several TCCON ground stations located in this region (e.g. Hefei, Saga, Tsukuba, Xianghe, Anmyeondo and Rikubetsu),  
125 as shown in Fig. 1, provide valuable ground-truth XCO<sub>2</sub> data for validating the MLP model predictions. If the model can  
accurately reproduce the TCCON observations from corresponding OCO-2 measurements, it suggests the model has learned  
meaningful relationships between the satellite data and underlying CO<sub>2</sub> concentrations.

Furthermore, the successful demonstration of accurate XCO<sub>2</sub> retrieval over East Asia is a first step toward expanding this  
approach globally. The model could be retrained or supplemented with additional regional data to extend coverage. By combin-  
130 ing reliable regional MLP models, global XCO<sub>2</sub> maps could be retrieved. This “jigsaw puzzle” strategy would further validate  
the feasibility of global-scale machine learning-based XCO<sub>2</sub> retrievals from satellite observations.

## 2.2 The artificial neural network architecture

This study introduces a multilayer perceptron (MLP) neural network model for estimating XCO<sub>2</sub> from OCO-2 satellite obser-  
vations. Inspired by David et al. (2021) and Bréon et al. (2022), the “MLP-XCO<sub>2</sub>” model input layer is designed based on the  
135 measurement principles of OCO-2 and atmospheric radiative transfer effects on the observed spectra, the artificial neural net-  
works architect is shown in Fig. 2. Specifically, the MLP model input layer consists of spectral information, surface pressure,  
the corresponding year, and geographical observation information as summarized in Table 1 and explained below.

**Spectral Information:** The OCO-2 satellite instrument measures high-resolution spectra in three spectral bands centered  
around 0.76, 1.6, and 2.0 μm, referred to as the O<sub>2</sub>-A, weak CO<sub>2</sub> (WCO<sub>2</sub>), and strong CO<sub>2</sub> (SCO<sub>2</sub>) bands, respectively (OCO-2  
140 Science Team et al., 2019). However, only the WCO<sub>2</sub> and SCO<sub>2</sub> bands are used as inputs for current XCO<sub>2</sub> retrievals. The O<sub>2</sub>-  
A band is excluded as it lacks significant information needed to directly estimate XCO<sub>2</sub>, based on radiative transfer principles.  
Instead, the O<sub>2</sub>-A band is primarily used in OCO-2’s operational full-physics algorithm for rapid cloud and aerosol screening  
prior to CO<sub>2</sub> retrieval (O’Dell et al., 2012), **effectively excluding observational cases that potentially lead to poor retrieval  
quality, thus** saving substantial computational costs. Each OCO-2 spectral band is sampled by 1024 detector pixels. However,

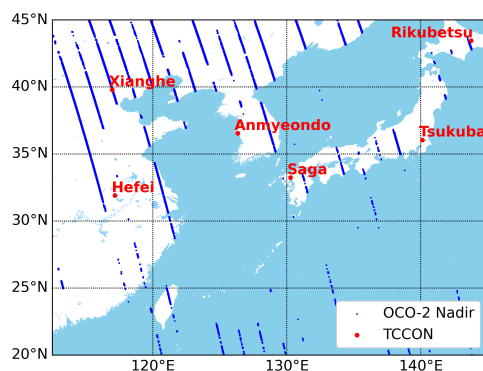


**Figure 1.** The target area for the East Asia region, distribution of observation points (from OCO-2 L2std v10r files) of OCO-2 Nadir mode  
in January 2016, and the distribution of TCCON sites in this area.

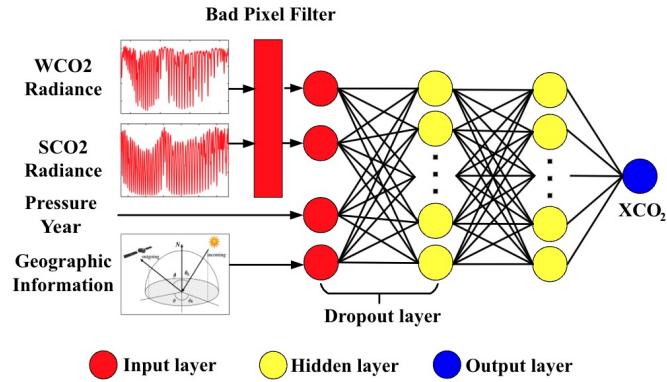


**Figure 2.** Schematic diagram of the MLP-XCO<sub>2</sub> model. The input layer includes two interpolated radiance of WCO<sub>2</sub> and SCO<sub>2</sub> band filtered through a bad pixel filter, geographical observation information, surface pressure, and the corresponding year. A dropout layer with a 0.1 dropout rate is added between the input layer and the first hidden layer.

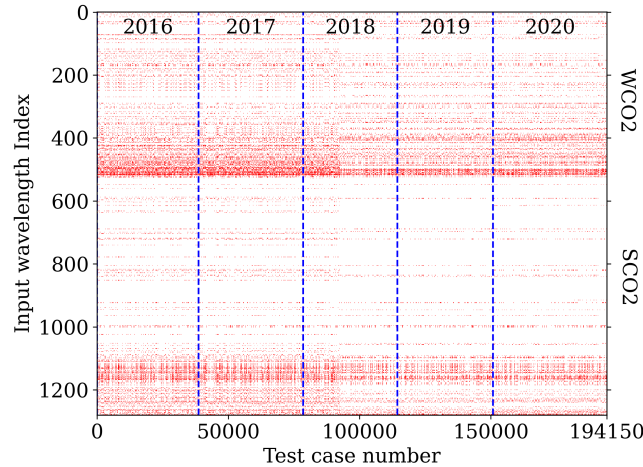


**Figure 3.** Visualization of the OCO-2 satellite data quality across wavelength grid indices. The map illustrates the bad sample list extracted from OCO-2 Level 1B files for all test cases. On the horizontal axis, sample numbers range from 0 to 194,150, while the vertical axis represents various wavelength grid indices, ranging from 0 to 1,280. Red coloration indicates problematic data pixels.

145 over time some detectors have degraded or become unstable in the space environment, resulting in pixels being flagged as “bad samples” in quality filters (Marchetti et al., 2019). To maximize high-quality training data, additional preprocessing is performed on the WCO<sub>2</sub> and SCO<sub>2</sub> bands. **Initially**, the beginning and ending spectral ranges corresponding to the most degraded detectors are removed. The remaining **good-quality** spectra are re-sampled into 525 and 755 wavelength points for the WCO<sub>2</sub> and SCO<sub>2</sub> bands, respectively (spectral points in wavelength are detailed in Table 2). To enhance the CO<sub>2</sub> absorption

**Table 1.** Detailed lists of the input parameters for the MLP-XCO<sub>2</sub> model

Input elements	Variables	Number
Spectral information	WCO <sub>2</sub>	525
	SCO <sub>2</sub>	755
	Bad pixel mask	1280
Geographical information	Solar zenith	1
	Relative azimuth	1
Others	Year	1
	Pressure	1
Total		2564

**Table 2.** Wavelength spacing of the input spectra

Band	Spectral range [ $\mu\text{m}$ ]	Spectral points [ $\mu\text{m}$ ]
WCO <sub>2</sub>	1.5990-1.6151	$\lambda_1 = 1.5990, \lambda_{i+1} = \lambda_i + 10^{-4} (6.10 - 3.60\lambda_i), i = 1-524$
SCO <sub>2</sub>	2.0478-2.0779	$\lambda_1 = 2.0478, \lambda_{i+1} = \lambda_i + 10^{-4} (7.58 - 3.48\lambda_i), i = 1-754$

150 line information, each input spectrum is normalized by dividing the mean radiance within a nearby spectrally transparent window lacking absorption features (1.6056-1.6059  $\mu\text{m}$  using 10 points for WCO<sub>2</sub>; 2.0602-2.0607  $\mu\text{m}$  using 15 points for SCO<sub>2</sub>). Additionally, as shown in Fig. 3, it's noticed that some isolated pixels within the main CO<sub>2</sub> absorption bands still consistently exhibit poor radiance quality. To address this issue, a 'bad sample filter' has been implemented, which utilizes a binary record from the OCO-2 L1B database (0 indicates spectra derived from good quality pixels, and 1 indicates pixels with defects or derived from poor quality interpolations). The settings of this filter are determined solely by the historic records and the version of the bad pixel map, ensuring refined data quality and consistency across different versions of the map. To further address bad samples resulting from natural degradation, we've implemented a dropout layer between the initial and the first intermediate MLP layer, thus enhancing the model's generalizability with the remaining spectral inputs.

**Geographical Information:** The model is designed to accept two key observation geometry angles that are determined by the relative positions of the Sun, satellite, and ground observation point. These include solar zenith angle and relative azimuth angle. The solar zenith angle (SZA) features prominently as a cosine term in the radiative transfer equation that defines the atmospheric radiative processes. Thus, SZA is pre-converted to its cosine form for model input. The relative azimuth angle is a comprehensive angle that jointly combines the solar azimuth angle and the satellite azimuth angle. It is important to emphasize that the satellite zenith angle is not utilized in this study. Our current research is based on the Nadir mode of the OCO-2 satellite observation. In the Nadir observing mode, the satellite zenith angle is assumed to be nearly perpendicular to the Earth's surface, theoretically approaching zero degrees.

**Other parameters:** In addition to the primary inputs, two other parameters play critical roles in the MLP-XCO<sub>2</sub> model: the surface pressure, and the corresponding year (e.g., 2016 or 2017, etc.). In traditional retrieval algorithms based on iterative optimization, accurate surface pressure and a reliable prior CO<sub>2</sub> profile are crucial. The importance of this has been highlighted by the averaging kernel utilized in the OCO-2 retrieval algorithm (Braverman et al., 2015), which indicates a higher sensitivity near the surface compared to the stratosphere. To prevent the retrieval of unrealistic CO<sub>2</sub> profiles, the prior covariance matrix imposes significantly stricter constraints in the stratosphere than in the troposphere (O'Dell et al., 2012). In cases where the prior CO<sub>2</sub> profile is inadequate, it can lead to poor results, with minimal or even opposite updates in the stratospheric CO<sub>2</sub> profile during the inversion process (Iwasaki et al., 2019). Additionally, in order to achieve the best agreement between observed and estimated spectra, the retrieval process may inaccurately estimate tropospheric CO<sub>2</sub> profiles. To tackle these challenges, our investigation suggests that incorporating additional information such as the “year” can offer valuable context for XCO<sub>2</sub> retrieval. This conservative approach provides a simple means to enhance prior CO<sub>2</sub> information without directly specifying XCO<sub>2</sub> prior values.

### 3 Satellite product data based machine learning model

In this section, we first developed the MLP-XCO<sub>2</sub> model using the OCO-2 v10r product dataset. The primary goal was to optimize the hyperparameters of the MLP-XCO<sub>2</sub> network. On one hand, we aimed to confirm whether the “slow bias”, as shown in Bacour et al. (2023) is a universal issue across machine learning models with similar architectures. On the other hand, by fixing the hyperparameters of the MLP-XCO<sub>2</sub> network structure, we sought to develop a comparable model using simulated data in later sections. In theory, MLP models using identical hyperparameters should possess the same fitting and generalization abilities. By first presenting results from a model trained solely on satellite product data, we can demonstrate the limitations of these satellite data-based models. This then motivates the development of new machine learning strategies to overcome these limitations, as discussed in later sections.

Following the target areas and data screening methods discussed previously, observational data and lists of bad pixels from the OCO-2 v10r L1B database. Additionally, retrieved surface pressure and XCO<sub>2</sub> data were obtained from the L2std database. Specifically, we obtained data from March, June, September and December spanning the years 2016 to 2020. This timeframe was chosen to provide a comprehensive training and testing set for our analysis. In total, the dataset encompassed 194150 samples collected over this five-year period. The year-wise distribution of the samples is as follows: 38626 samples from 2016, 39850 from 2017, 35945 from 2018, 36452 from 2019, and 43277 from 2020.

~~Before training the MLP-XCO<sub>2</sub> model, we should first focus on the development and training of the MLP-P model, which is crucial for accurate surface pressure retrieval and subsequent input into the MLP-XCO<sub>2</sub> model. The MLP-P model, with only {500, 200, 50} hidden layer nodes and the same input layer composition as the MLP-XCO<sub>2</sub>. All hidden layers use ReLU activation functions. Trained on historical OCO-2 product data from 2016 to 2018, the MLP-P model has demonstrated the ability to provide stable predictions of surface pressure for the years 2019 to 2020, as illustrated in Fig. ??.~~



After completing the data collection, we proceeded to construct the MLP-XCO<sub>2</sub> model. To balance model complexity and performance, the MLP-XCO<sub>2</sub> architecture (Fig. 2) comprises five hidden layers, with 1000, 500, 300, 100 and 20 nodes, respectively. All hidden layers also use ReLU activation functions. The output layer contains a single node to predict XCO<sub>2</sub> values, with a linear activation function. Upon developing the MLP-XCO<sub>2</sub> model architecture, in this section, we independently trained two versions of the MLP-XCO<sub>2</sub> model, each based on the aforementioned model structure but with different training and testing datasets.

**Historical Data Training:** The first MLP-XCO<sub>2</sub> model based on OCO-2 product data was trained using historical XCO<sub>2</sub> collected from 2016 to 2018. The test set for this model comprised product data from the years 2019 and 2020. This setup allows us to assess the model's predictive performance using a straightforward historical data approach.

**Skipped-Year Training:** The second version of the model was trained using data from the years 2016, 2018, and 2020. The test set for this MLP-XCO<sub>2</sub> model included the skipped years, 2017 and 2019. This unique approach enables a clearer and more direct comparison of the potential limitations of relying solely on historical data for future predictions.

Figure 4 presents the results for the two trained MLP-XCO<sub>2</sub> models on their respective 10% out-of-sample testing datasets. The first subplot illustrates the predictions of the historical data training model from the 2016-2018 data, and the second subplot shows similar predictions for the skipped-year training model. Both models achieve high accuracy on these testing datasets, with a Root Mean Square Error (RMSE) close to 1 ppm and an R-squared score (R<sup>2</sup>) larger than 0.9. These results demonstrate the robust interpolation capabilities of both models within their respective training periods, indicating their effectiveness in handling known observed scenarios.

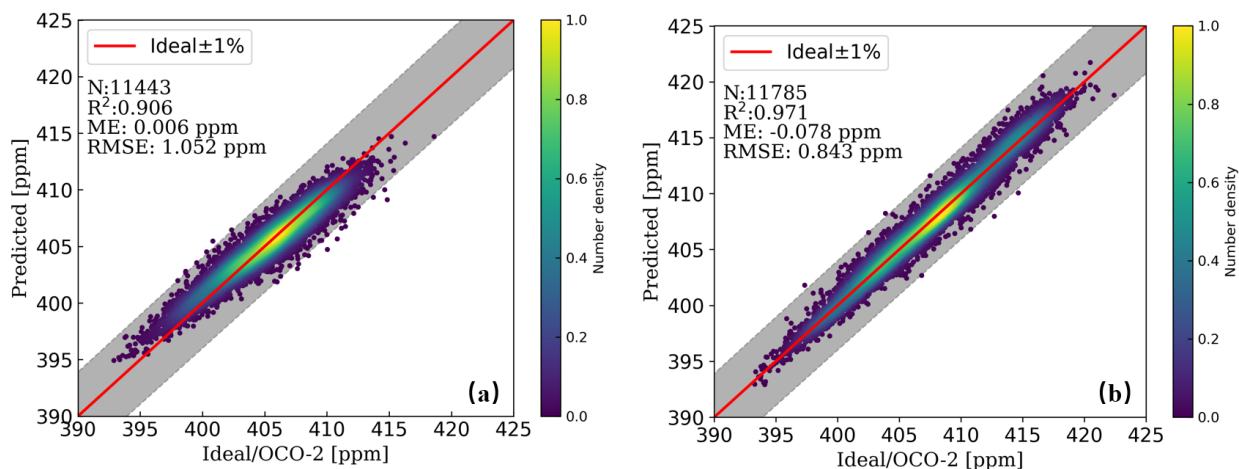


**Figure 4.** Comparison of 10% out-of-sample XCO<sub>2</sub> testing cases predicted by the MLP-XCO<sub>2</sub> model versus results retrieved by OCO-2 v10r product. Panel (a) is for the historical data training model, while (b) is for the skipped-year training model. The solid red lines in the figure correspond to the perfect agreement, where shadow areas around the solid red lines represent ±1% of XCO<sub>2</sub> deviations.

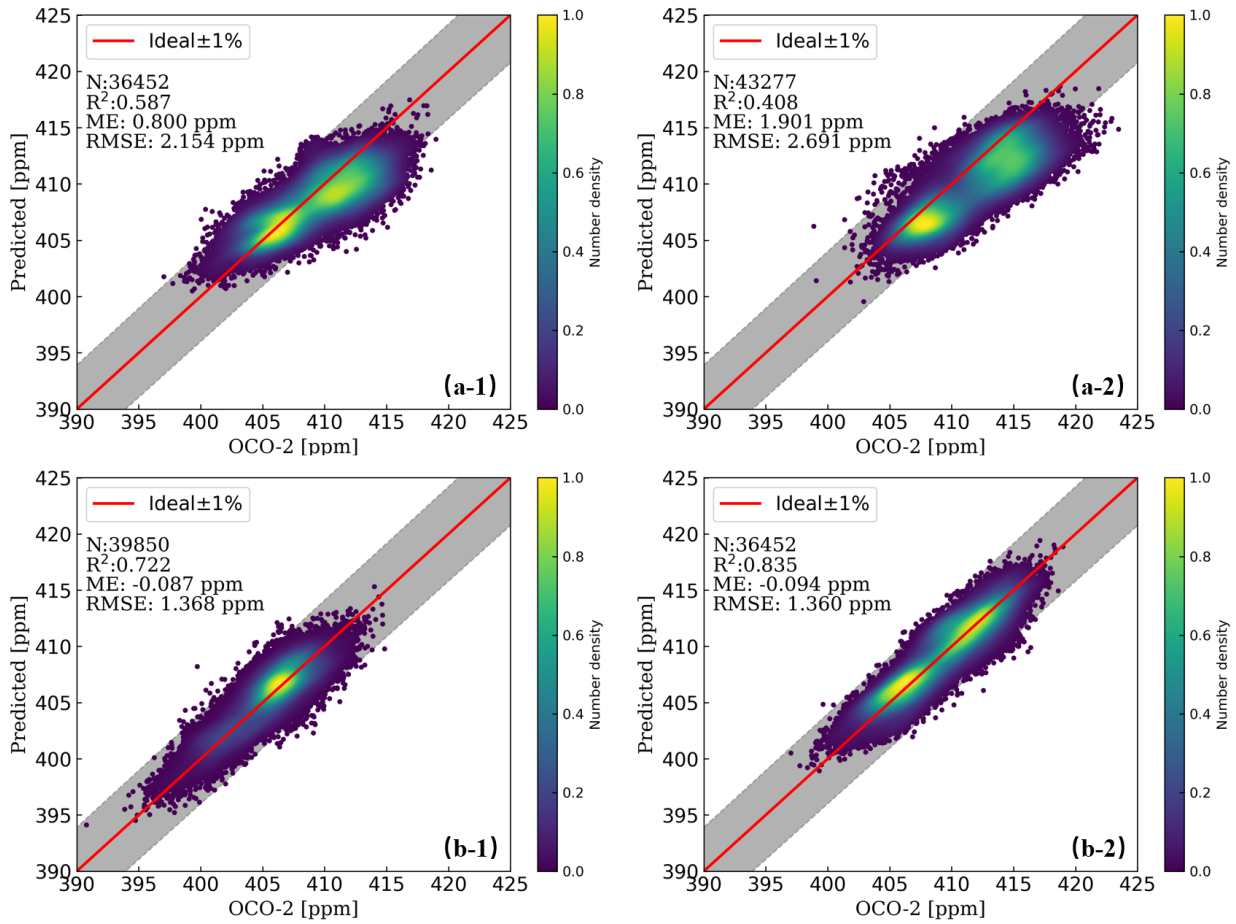


**Figure 5.** Comparison of XCO<sub>2</sub> results predicted by the MLP-XCO<sub>2</sub> model versus results retrieved by OCO-2 v10r product on test sets consisting of years not included in the training periods. Panels (a-1) and (a-2) are for the historical data training model on the 2019 and 2020 test sets, respectively. Panels (b-1) and (b-2) are for the skipped-year training model on the 2017 and 2019 test sets, respectively. The solid red lines in the figure correspond to the perfect agreement, where shadow areas around the solid red lines represent ±1% of XCO<sub>2</sub> deviations.

Figure 5 evaluates the generalization capabilities of each MLP-XCO<sub>2</sub> model on testing sets comprising years not included in their respective training datasets. These test sets represent periods outside the range of years used for training. Here, we solely observed a noticeable positive bias in the predictions from the historical data training model. In contrast, the skipped-year training model did not exhibit this bias. Performance remains highly accurate on these out-of-range points, further validating the model's robustness for XCO<sub>2</sub> prediction within skipped years.

Globally, the average XCO<sub>2</sub> in the atmosphere shows a stable annual increase, with an observed rise of approximately 2-3 ppm per year. However, despite the inclusion of the corresponding year in the input layer as a high-correlation parameter,

there remains a limitation in capturing the atmospheric CO<sub>2</sub>'s potential rising trend. This highlights the limitations of models trained solely on historical satellite data, motivating the development of new techniques to incorporate external information about temporal CO<sub>2</sub> dynamics.

#### 4 Simulation data based machine learning model

In the previous section, the MLP-XCO<sub>2</sub> model showed excellent interpolation within the training data range but exhibited bias when predicting outside this period. To eliminate this bias, we propose using an accurate forward model to simulate representative training data that covers future atmospheric conditions. If we can pre-generate atmospheric profiles that capture possible future states, and simulate their corresponding spectral radiance using an accurate forward model, the MLP-XCO<sub>2</sub> model can pre-learn future satellite observations. This could prevent the incremental annual bias and enable accurate XCO<sub>2</sub> prediction. The effectiveness of this approach depends on the forward model accuracy and representativeness of the simulated atmospheres (Zhao et al., 2022).

It is therefore critical to select an appropriate radiative transfer forward model with proven reliability in simulating spectral radiance under varying atmospheric conditions. The model must precisely capture the relationship between trace gas concentrations, meteorological states, and resulting spectral signatures. With accurate simulations, the machine learning model can generalize robustly to future atmospheric scenarios. The representative training data should span the expected range of atmospheric variability in XCO<sub>2</sub> and interfering species like water vapor. A broad sampling of the state space is key for the model to learn a robust mapping to XCO<sub>2</sub> across multiple atmospheric regimes. The following sections describe our approach for accurate spectral radiative transfer simulations and possible (realistic) atmospheric profile generations.

##### 4.1 Forward model

In this study, we developed a forward radiative transfer calculation model using the ReFRACtor (Reusable Framework for Retrieval of Atmospheric Composition) software (McDuffie et al., 2018). ReFRACtor is an extensible framework for multi-instrument atmospheric radiative transfer and retrieval, originally derived from the operational OCO-2 retrieval program. Although ReFRACtor contains both radiative transfer and retrieval capabilities, we only utilized the radiative transfer component. Specifically, we configured ReFRACtor to simulate top-of-atmosphere radiance spectra that would be observed by OCO-2. These simulated observations were then used to generate a large training dataset for our machine learning model, MLP-XCO<sub>2</sub>.

The OCO-2 satellite primarily observes the radiative spectra in the short-wave infrared (SWIR) band. Over the range of SWIR, the impact of thermal emission can be ignored when simulating the spectra (Crisp et al., 2021). To simulate OCO-2's observed spectra in the WCO<sub>2</sub> band around 1.6 μm and the SCO<sub>2</sub> band around 2.06 μm, the ReFRACtor model numerically solves the Eq. (1) of the radiative transfer equation (RTE) (Modest and Mazumder, 2021):

$$\mu \frac{dI(\tau, \mu, \phi)}{d\tau} = -I(\tau, \mu, \phi) + J(\tau, \mu, \phi) \quad (1)$$

where  $I_\eta$  is the observed spectra,  $\mu$  is the cosine of the observation zenith angle (e.g.,  $\mu = \cos\theta$ ),  $\tau$  is the vertical optical depth which can be column-integrated from the molecular absorption coefficients and optical path,  $\phi$  is the azimuthal angle relative to the observation point for the satellite and the sun, and  $J$  represents the scattering components and inhomogeneous source term, describing both single scattering and multiple scattering contributions. The term  $J$  in RTE can be expressed as Eq. (2):

$$J(\tau, \mu, \phi) = \frac{\omega}{4\pi} \int_{-1}^1 \int_0^{2\pi} P(\tau, \mu, \phi; \mu', \phi') I(\tau, \mu', \phi') d\mu' d\phi' + \frac{\omega}{4\pi} P(\tau, \mu, \phi; \mu', \phi') I_0 \exp(-\tau/\mu_0) \quad (2)$$

where  $\omega$  is the single scattering albedo,  $P$  is the scattering phase function,  $\mu'$  and  $\phi'$  are the cosine and azimuth angle of the incident direction angle in each direction,  $\mu_0$  is the cosine of the solar zenith, and  $I_0$  is the solar intensity in the top of the atmosphere.

The ReFRACtor model uses a hybrid model to solve RTE. Specifically, the radiative transfer software LIDORT (Spurr, 2008) is applied for the scalar and Jacobian computation. Concurrently, the two-order scattering model (Natraj and Spurr, 2007) is utilized for the additional radiance correction. Within this framework, the ReFRACtor model comprehensively considers five types of scatter particles for each sounding: two types of clouds, two types of tropospheric aerosols, and one type of stratospheric aerosol. The single scattering optical properties for each cloud and aerosol particle, including cross-section, single scattering albedo, and scattering phase matrix, have been pre-computed and tabulated for the forward calculations. Furthermore, the model determines surface reflectance as a quadratic spectral albedo for each band which is derived from the bidirectional reflectance distribution function (BRDF).

An essential step for developing the forward calculation model is referencing the pre-computed look-up table of H<sub>2</sub>O and CO<sub>2</sub> to obtain the required spectral absorption coefficients. In this study, the ABSCO v5.1 database (Absorption Coefficient Table (Payne et al., 2020)) was applied for this purpose. Additionally, we identified and corrected an overestimation of the solar continuum in ReFRACtor compared to the OCO-2 Level 2 algorithm (Crisp et al., 2021). Without this correction, there would have been approximately 3 % overestimation in the 1.6  $\mu\text{m}$  band and 6.5 % in the 2.06  $\mu\text{m}$  band. By reducing the solar continuum, our forward model aligned better with the OCO-2 spectral measurements. These configurations of the absorption coefficients and solar continuum were essential to accurately simulate OCO-2 spectra for generating training data across a variety of observing conditions.

To assess the performance of the forward model, we selected four distinct global locations in the year of 2017. The goal was to replicate the OCO-2 observed spectra for both the WCO<sub>2</sub> 1.6  $\mu\text{m}$  absorption band and the SCO<sub>2</sub> 2.06  $\mu\text{m}$  absorption band at the four locations. By accessing the OCO-2 L2std database, we acquired atmospheric conditions and pertinent geographical data (including spectral albedo, surface pressure, and observation angles) specific to these chosen locations. The outcomes of our simulations for these four locations are visually depicted in Fig. 6 and Fig. 7, respectively for the two bands, with accompanying residual plots displayed in the lower panels. It is worth noting that the simulated results exhibit a high level of agreement with the observed OCO-2 spectra; the relative error remains under 1%, underlining the robustness of the established forward model. The remarkable agreement between the observed and simulated spectra indicates the excellent performance of the forward radiative transfer model. This performance is particularly evident in accurately replicating the satellite observations

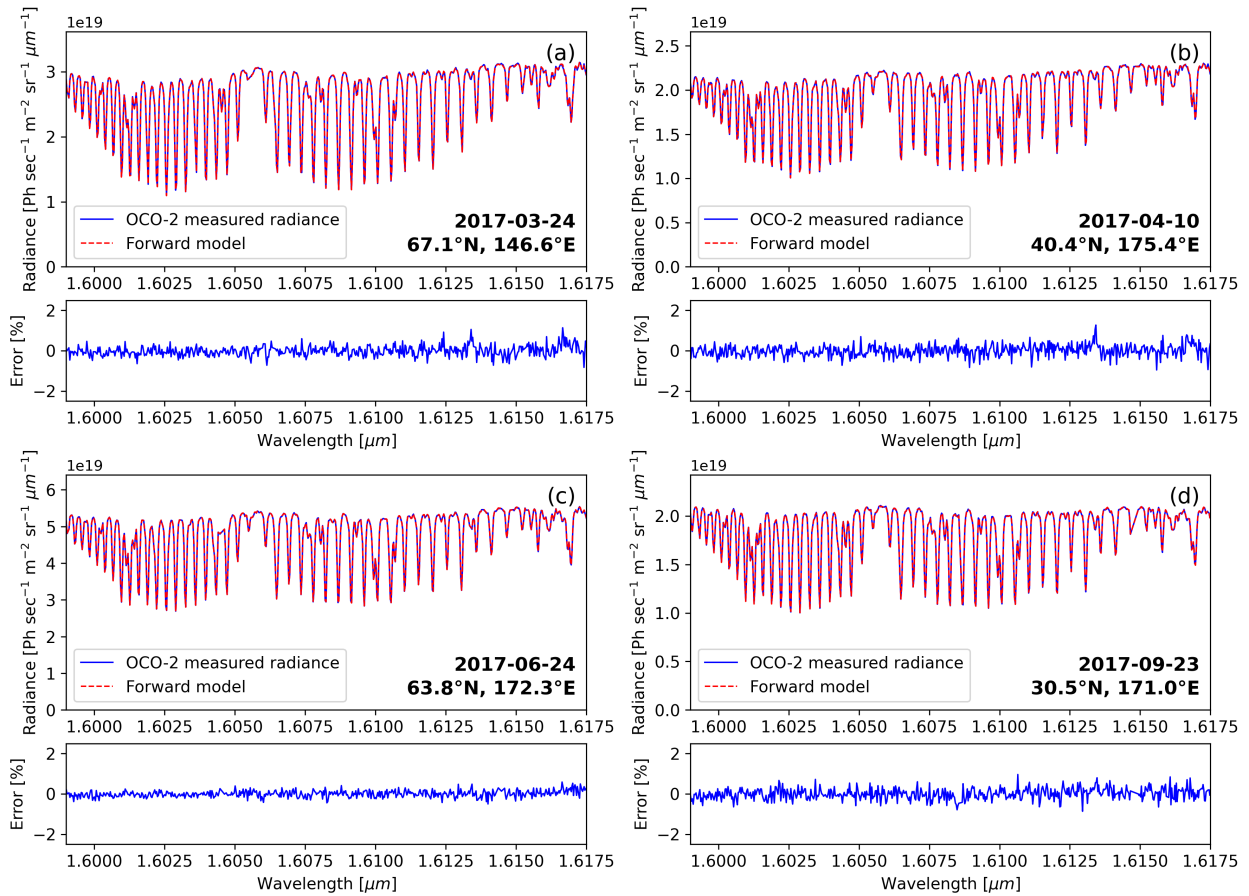


**Figure 6.** Comparisons of the OCO-2 observed spectra with the simulated ones from the modified ReFRACtor forward calculation model in WCO<sub>2</sub> band. The lower panel shows the relative error between the spectrum observed by the OCO-2 satellite and that simulated by the forward calculation model. Subplots (a)-(d) correspond to test samples from four different regions. The input vectors for the ReFRACtor model were derived from OCO-2 L2std retrieved results.

from OCO-2. As a result, this forward model serves as a reliable tool for the development of machine learning models trained using simulated spectral data.

## 4.2 Training data generation

290 To optimize the training of the MLP-XCO<sub>2</sub> model, it is essential that the input training vectors cover a wide range of realistic variations. Although the idea of randomizing all input parameters to enhance diversity might appear attractive, simulating satellite spectra involves managing a multitude of interdependent variables. In addition to the CO<sub>2</sub> vertical profile, factors such as surface pressure, temperature profile, water vapor, aerosols, and observation geometry must be accurately represented. Randomizing all of these parameters would require an impractical amount of data and could result in combinations that have

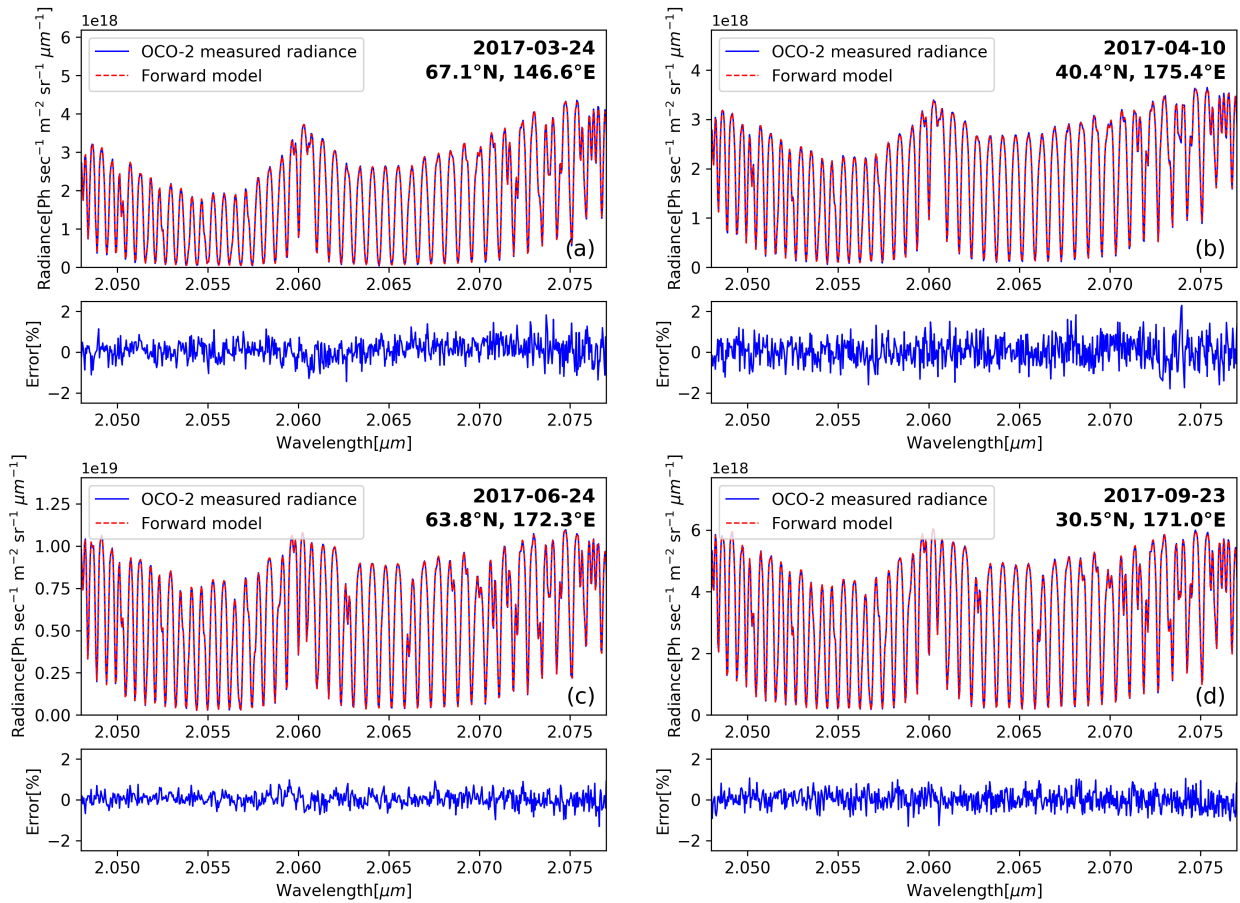


**Figure 7.** Comparisons of the OCO-2 observed spectra with the simulated ones from the corrected ReFRACtor forward calculation model in SCO<sub>2</sub> band. The lower panel shows the relative error between the spectrum observed by the OCO-2 satellite and that simulated by the forward calculation model. Subplots (a)-(d) correspond to test samples from four different regions. The input vectors for the ReFRACtor model were derived from OCO-2 L2std retrieved results.

295 no real-world relevance. For example, the four viewing angles determined by the sun, observation point, and the OCO-2  
satellite have fixed combinations during the satellite’s regular operation. Therefore, randomly selecting angle combinations  
lacks practical significance. To ensure that the training data covers valid variations, we conducted an analysis of historical  
OCO-2 retrievals. This analysis revealed consistent seasonal patterns and year-to-year trends in most parameters. This supports  
the idea of selecting representative samples from statistical distributions rather than relying on complete randomization. By  
300 carefully considering the relationships between parameters and the realities of satellite observations, we can create a reasonably  
sized training dataset that effectively captures the range of expected predictions.

The generation of the vertical CO<sub>2</sub> profile is especially critical among all input parameters. This dataset theoretically de-  
termines the generalization domain of the MLP-XCO<sub>2</sub> model. In the forward model based on the ReFRACtor model, the

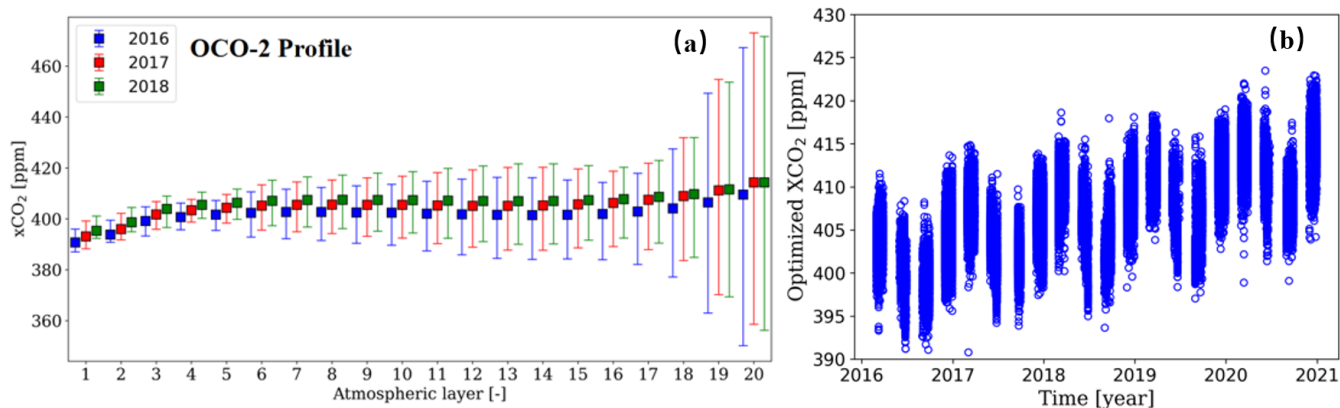


**Figure 8.** Panel (a) is the boxplot of the vertical distribution of CO<sub>2</sub> profiles (from OCO-2 L2std files) retrieved by the OCO-2 satellite over East Asia in Nadir mode from 2016 to 2018. The horizontal axis represents the atmospheric layers from layer 1 (top of the atmosphere) to layer 20 (near-surface). The upper and lower bounds of each box show the maximum and minimum CO<sub>2</sub> concentrations recorded within that layer for each year. Panel (b) is the scatter plot of historic XCO<sub>2</sub> results retrieved by the OCO-2 inversion program (from L2std files)

atmospheric CO<sub>2</sub> profile is segmented into 20 sub-layers by pressure. By statistically analyzing the OCO-2 retrieved CO<sub>2</sub> profiles in the target East Asia area from 2016-2018, the box plots for atmospheric CO<sub>2</sub> concentration in each sub-layer are shown in Fig. 8(a), and the historic XCO<sub>2</sub> results from the OCO-2 product data are showing in Fig. 8(b). From the upper atmosphere down to the ground surface, the variability of CO<sub>2</sub> concentrations gradually increases. This challenges the ability for the standardization of atmospheric CO<sub>2</sub> profiles, particularly closer to the Earth's surface. Fortunately, a consistent year-on-year rise in CO<sub>2</sub> concentrations in each sub-layer has been observed over time. Consequently, in our research, we have proposed a method for generating subsequent CO<sub>2</sub> atmospheric profiles. We incrementally increase the CO<sub>2</sub> concentration by 2.5 ppm annually, starting from the 2016 OCO-2 retrieved CO<sub>2</sub> vertical profile. This approach ensures that we encompass a range of plausible atmospheric CO<sub>2</sub> distributions with realistic shapes, enabling the generation of simulated spectra for the designated training years.

In addition to the CO<sub>2</sub> profile, Fig. 9 illustrates the year-to-year trends of various observed parameters essential for the forward calculation model in the East Asian region. These parameters, although they display seasonal variations, consistently exhibit annually cyclic patterns. Given that the OCO-2 satellite conducts global observations in cycles of approximately half a month (15-16 days), this study employed observation parameters and priori data for atmospheric profiles, except for CO<sub>2</sub>, from the year 2016 as a reference. These reference data were repetitively utilized for generating simulations in subsequent years. Regarding the quadratic spectral albedo, the constant term in the training data samples is uniformly set to 1 (to be normalized before being processed by the neural network). The slope and the quadratic coefficient are stochastically sampled within the range of values corresponding to the retrieval results based on the OCO-2 L2 products.

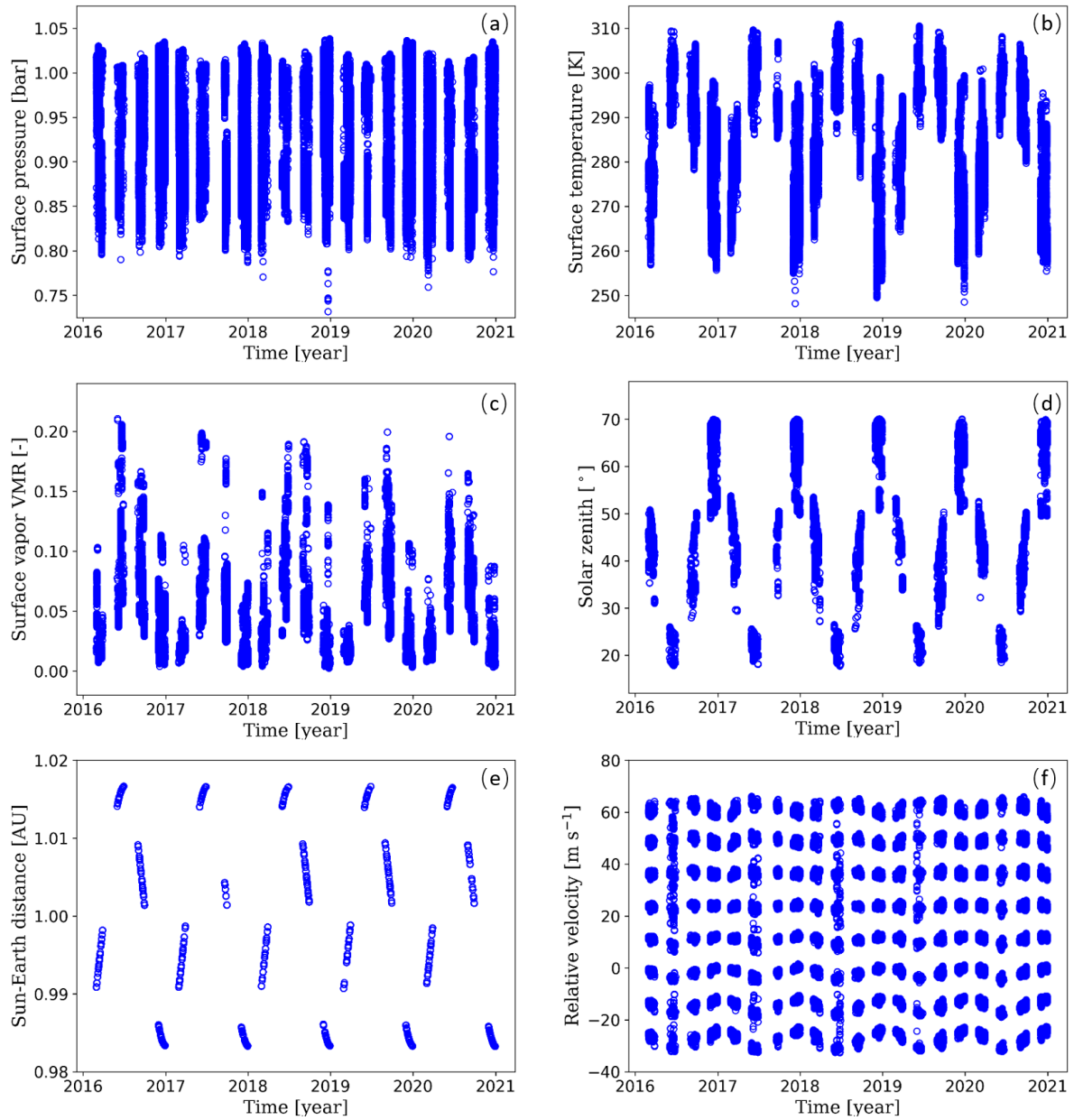


**Figure 9.** Scatter plots of atmospheric parameters required for forward calculation models (excluding CO<sub>2</sub> profiles) from 2016 to 2020, sourced from the OCO-2 L2 product. Panel (a) is the surface pressure, (b) is the surface temperature, (c) is the near-surface water vapor concentration, (d) is the solar zenith, (e) is the Sun-Earth distance, and (f) is the Earth-satellite relative velocity.

Based on 60,000 uniformly sampled observation data points exclusively from the OCO-2 satellite throughout 2016, we randomly separated it into six sets of 10,000 data points each. Each set represents CO<sub>2</sub> profiles from 2016 to the end of 2021,



with a yearly increase of 2.5 ppm added to the original data, reflecting projected future profiles. The forward model was used  
325 to generate the corresponding simulated spectra for each set. These simulated samples serve as the foundational dataset for  
training the new MLP-XCO<sub>2</sub> machine learning model. It's important to note that this new model relies solely on the data  
recorded by the OCO-2 satellite in 2016, as its reference. However, it is essential to acknowledge that real-world observations  
by the OCO-2 satellite involve parameters that are not predetermined in future simulations, such as the Empirical Orthogonal  
Functions (EOF) parameters, signal-to-noise ratio (SNR), bad sample lists, and the degradation of grating pixels. Therefore,  
330 our new model is trained not only on the 60,000 simulated datasets but also on the 2016 historical data. According to the data  
selection criteria outlined in Section 2.1, we identified a total of 38,626 sets of historical data in 2016, comprising spectral  
measurements from OCO-2 and the corresponding XCO<sub>2</sub> products. These historical experimental datasets are integrated with  
the simulated data, enriching the training datasets. This dual combination and data augmentation techniques ensure that the  
model is well-equipped to handle both potential future atmospheric conditions and the current realities of instrument and  
335 spectral measurement capabilities. By doing so, we provide a more comprehensive training strategy that captures both the  
anticipated future scenarios to accurately and efficiently perform XCO<sub>2</sub> retrieval for the “future” years from 2017 to the end of  
2020.

## 5 Results and discussions

### 5.1 Comparison with the OCO-2 satellite product data

340 To evaluate the retrieval capability of the MLP-XCO<sub>2</sub> model trained on a combined dataset of simulated data and historical  
2016 OCO-2 satellite data, the neural network architecture and hyperparameters were intentionally kept identical to the pre-  
vious model trained solely on actual OCO-2 satellite product data. Keeping these factors constant isolates the training data  
source as the only major difference between the models. This enables a direct, apples-to-apples comparison of how the training  
data affects model performance.

345 Figure 10 (a) shows the retrieval results on 10% out-of-sample testing data that was excluded from model training. Setting  
aside this test subset is a standard technique for evaluating model performance on new examples. The accurate predictions  
of the MLP-XCO<sub>2</sub> model on the test data suggest the model has learned generalizable patterns not overfit to the training  
data. Figure 10 (b) shows the comparison of the retrieval results of the MLP-XCO<sub>2</sub> model on real OCO-2 satellite spectral  
observations in 2016. Figure 11 displays XCO<sub>2</sub> predictions from 2017 to 2020 using test data consistent with Fig. 4 and Fig. 5.  
350 As the simulated training data was generated based on 2016 OCO-2 measurements, testing on 2017-2020 data evaluates the  
model's ability to make predictions beyond the time frame of the training data. The scatter plots demonstrate the MLP-XCO<sub>2</sub>  
model trained on simulated data can accurately and stably predict the annual XCO<sub>2</sub> growth trend, maintaining RMSE **less than  
1.8 ppm (0.45%)**. Compared to models trained relying solely on historical satellite product data, the key advantage is the ability  
to make reasonable forecasts of future atmospheric XCO<sub>2</sub> levels.

355 Table 3 offers a detailed spatio-temporal comparison of the results presented in Figure 11, enhancing our understanding of the  
MLP-XCO<sub>2</sub> model's performance across distinct subregions within East Asia. This table specifically focuses on a finer spatial

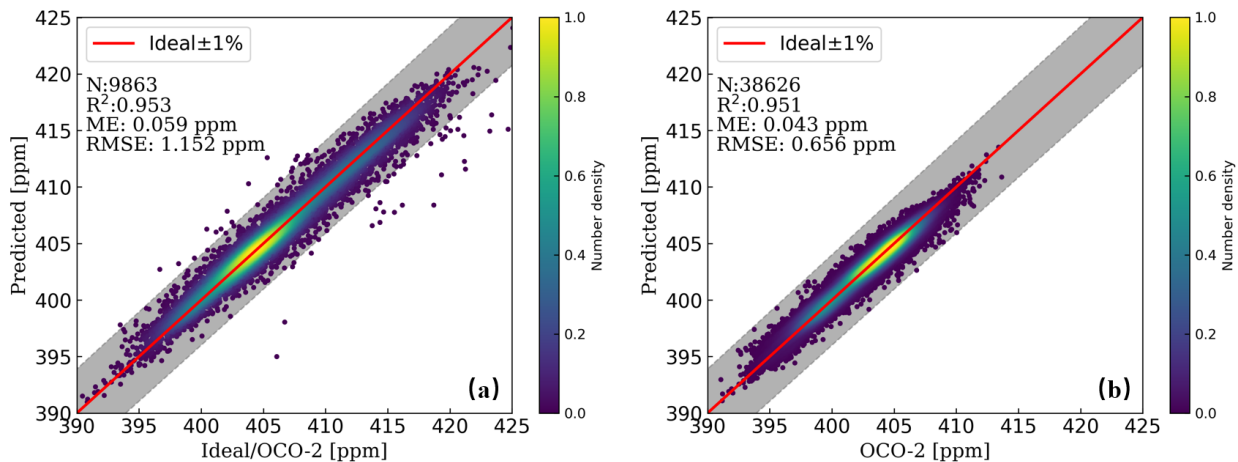


**Figure 10.** The comparison of XCO<sub>2</sub> results predicted by the MLP-XCO<sub>2</sub> model from 10% test data (not involved in training). Panel (a) shows the predicted XCO<sub>2</sub> values for the test data that are derived from the simulated dataset, and panel (b) shows the test data that are derived from OCO-2 2016 L2 XCO<sub>2</sub> data.

segmentation within the broad East Asian longitude and latitude range, dividing it into four subregions. These are defined based on the geographical demarcation of 35°N and 130°E, categorized as Northeast (NE), Northwest (NW), Southeast (SE), and Southwest (SW) regions, respectively. The results demonstrate that, regardless of the distribution of sample sizes across these subregions and their varied topographical characteristics (land or ocean), the model maintains a consistent and stable performance in each subregion. Furthermore, the error metrics for these individual subregions align closely with the overall regional errors, indicating a uniformity in the model’s predictive accuracy and reliability across different spatial scales within East Asia.

Considering these results, by generating possible realistic future prior information for the atmospheric conditions and using an accurate forward model to simulate the corresponding spectra, the approach avoids inherent biases when extrapolating beyond the distribution of the training data. Rather than simply extending trends, the model is constrained by fundamental physical relationships to interpolate within realistic bounds. This transforms the prediction task into a well-posed interpolation problem versus an unconstrained extrapolation. The simulated data provides a physical regularization that makes the model’s outputs to be scientifically sound. By training on synthetic data spanning potential future scenarios, the model learns robust representations not tightly coupled to specifics of the training data time period. This enables high-fidelity inversion and prediction of XCO<sub>2</sub> even for future time periods beyond available measurements.

## 5.2 Detecting plume features from the OCO-2 observation

In a further effort to deeply analyze the ability of our MLP-XCO<sub>2</sub> model to capture key XCO<sub>2</sub> information from spectral data, we focused on plume detection at sites of potentially high emissions, such as thermal power plants, in our target regions from

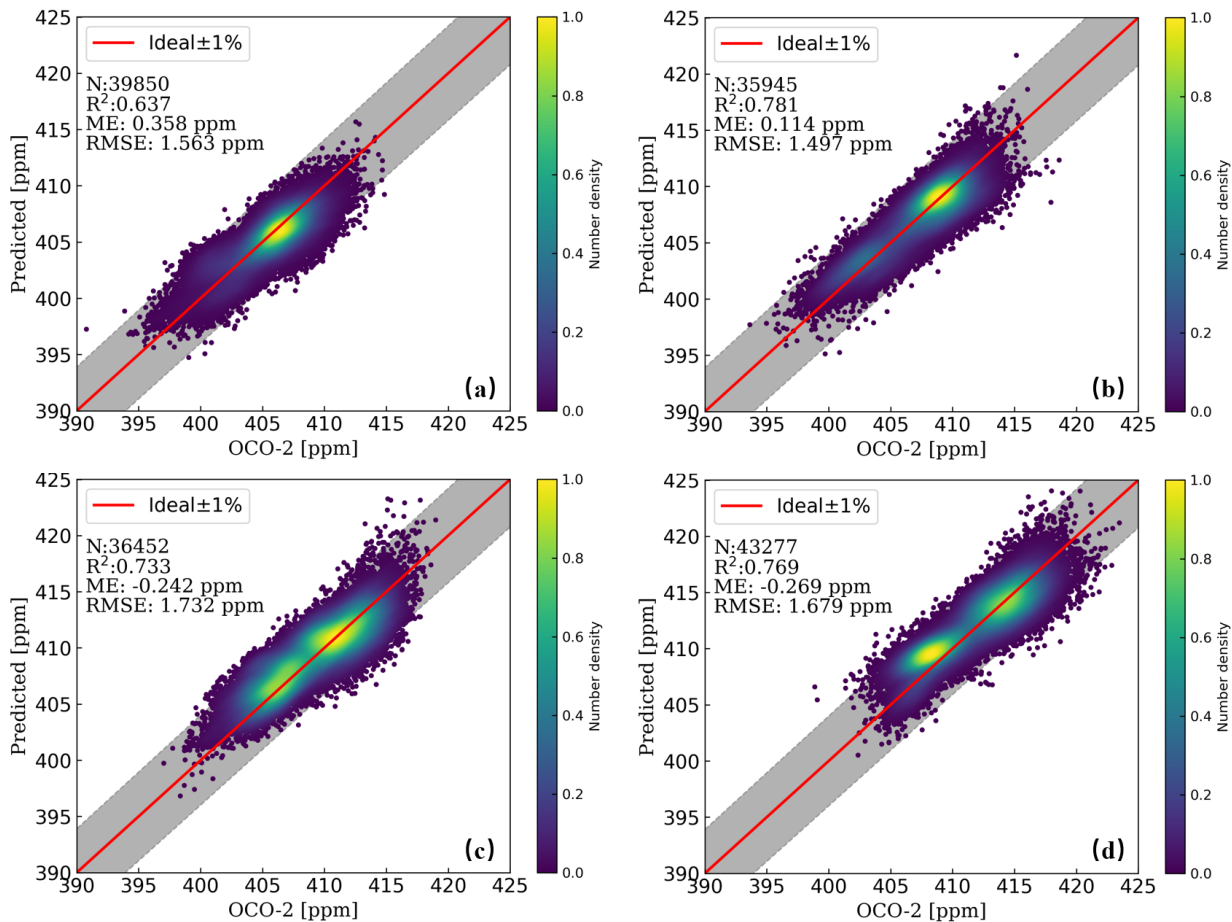


**Figure 11.** Comparison of XCO<sub>2</sub> results predicted by the MLP-XCO<sub>2</sub> model versus results retrieved by OCO-2 v10r product from 2017-2020. Panel (a), (b), (c), and (d) display the predictions of the MLP-XCO<sub>2</sub> model from 2017 to 2020, respectively.

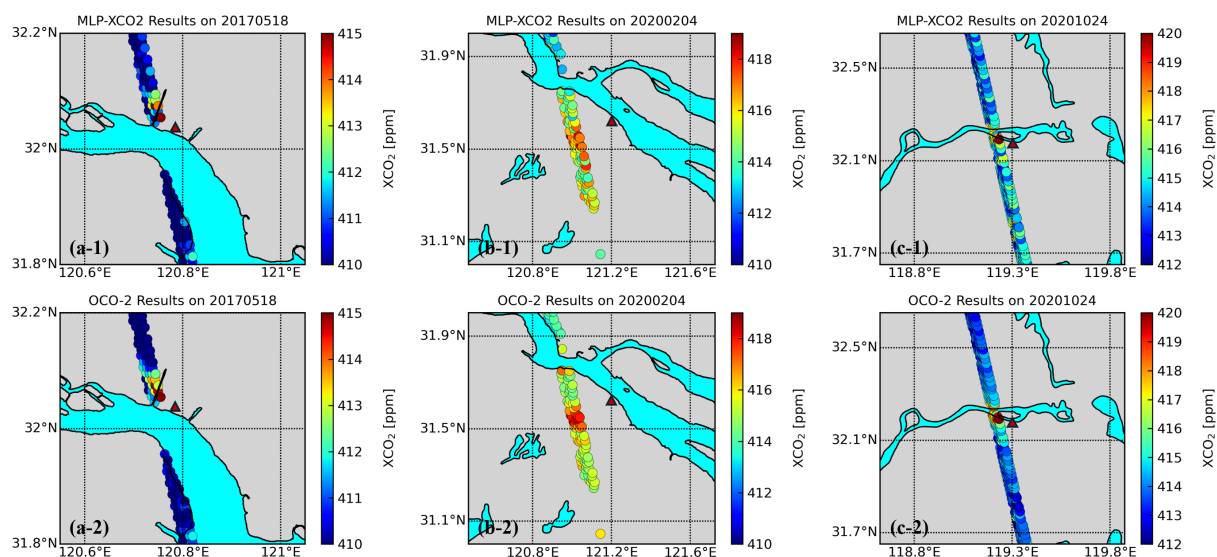
375 2017 to 2020. Utilizing the data in the work of Li et al. (2023), we sourced test samples from multiple instances of XCO<sub>2</sub> enhancements detected by the OCO-2 satellite in Nadir mode observations. These samples were located in close proximity to known large power plants, providing an ideal scenario for assessing retrieval accuracy in detecting localized emission sources.

Figure 12 presents a geographical map that highlights XCO<sub>2</sub> predictions in the test samples from the MLP-XCO<sub>2</sub> model and compares them with results retrieved by the OCO-2 v10r product. This map clearly marks power plants with red triangles, establishing a visual link between industrial emission sources and observed points where elevated XCO<sub>2</sub> levels are detected.  
 380 Figure 13 further explores this relationship by presenting a longitude-based comparison of XCO<sub>2</sub> results. This figure plots the same data points from Figure 12 against their corresponding longitude coordinates. This arrangement facilitates a direct and intuitive comparison of the trends in XCO<sub>2</sub> enhancements as captured by our model and as reported by the OCO-2 product.

**Table 3.** Spatio-temporal comparison of XCO<sub>2</sub> predicted by MLP-XCO<sub>2</sub> model results versus results retrieved by OCO-2 across four subregions. These subregions are delineated based on the geographical demarcation of 35°N and 130°E as: Northeast (NE), Northwest (NW), Southeast (SE), and Southwest (SW) regions, respectively.

Year	Full [Number / ME / RMSE]	NE	NW	SE	SW
2016	38626 / 0.043 / 0.656	2714 / -0.037 / 0.600	26111 / 0.053 / 0.664	451 / 0.010 / 0.583	9350 / 0.041 / 0.651
2017	39850 / 0.358 / 1.563	1235 / 0.752 / 1.494	30774 / 0.392 / 1.594	244 / 0.701 / 1.537	7597 / 0.147 / 1.443
2018	35945 / 0.114 / 1.497	1854 / -0.073 / 1.356	27288 / 0.145 / 1.483	745 / 0.525 / 1.398	6058 / -0.015 / 1.609
2019	36452 / -0.242 / 1.732	1777 / -0.642 / 1.552	26082 / -0.427 / 1.863	304 / 0.345 / 1.432	8289 / 0.405 / 1.296
2020	43277 / -0.268 / 1.679	1841 / 0.111 / 1.586	34971 / -0.461 / 1.696	270 / -0.413 / 1.917	6195 / 0.712 / 1.595

In both figures above, it is visually evident that observation points near power plants show sudden increases in XCO<sub>2</sub> values, aligning with the trend from the OCO-2 v10r product. This trend is particularly pronounced when compared to points farther away from these emission sources. Considering that these samples are nearly identical in terms of observation angles and times, such consistency is a powerful confirmation to our model's capability to retrieve genuine atmospheric XCO<sub>2</sub> from OCO-2 spectral data.



**Figure 12.** Geographical map of XCO<sub>2</sub> predictions by the MLP-XCO<sub>2</sub> model compared with OCO-2 v10r product results. The potential plume enhancements and the large power plants (marked by red triangles) were screened in Nadir mode OCO-2 observations as reported in the work of Li et al. (2023).

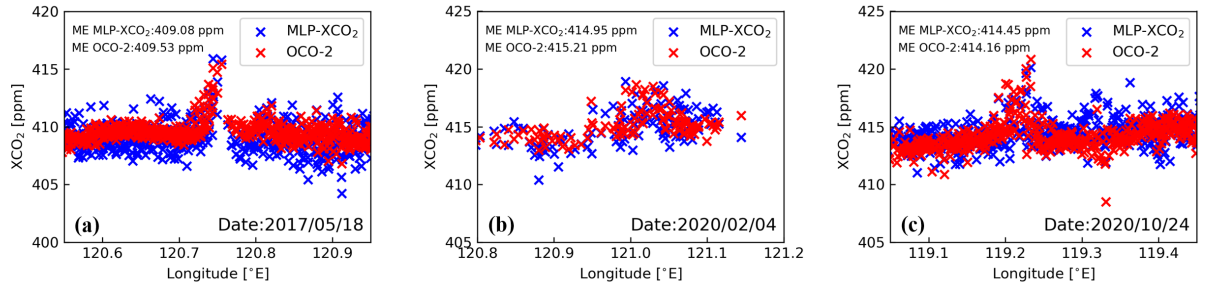


**Figure 13.** Longitude-based scatter comparison of XCO<sub>2</sub> predicted by the MLP-XCO<sub>2</sub> model versus results retrieved by OCO-2 v10r product. The potential plume enhancements were screened in Nadir mode OCO-2 observations as reported in the work of Li et al. (2023). ME represents the mean value of XCO<sub>2</sub> within the longitude range shown in the figure.

### 5.3 Comparison with the TCCON data

390 A comparison of the retrieved results from the OCO-2 satellite showed that the RMSE of our developed MLP-XCO<sub>2</sub> model was around 2 ppm. In other words, our results could be worse or better than OCO-2 satellite, requiring further comparison with ground-based measurements. To further validate the accuracy of the MLP-XCO<sub>2</sub> model, we compared the XCO<sub>2</sub> retrievals from the OCO-2 v10r Nadir mode products, the MLP-XCO<sub>2</sub> model outputs, and ground-based measurements from five TCCON sites within the study region (Fig. 1). As summarized in Table 4, spatiotemporal screening was applied to the TCCON  
 395 and OCO-2 data to obtain comparable observations. The five TCCON sites included were: Tsukuba (Morino et al., 2022b), Saga (Shiomi et al., 2022), Hefei (Liu et al., 2022), Xianghe (Zhou et al., 2022) and Rikubetsu (Morino et al., 2022a). The Anmyeondo site was excluded from this analysis as the XCO<sub>2</sub> data was not updated in the TCCON GGG2020 database, and was only available until early 2018 in the GGG2014 database.

**Table 4.** Spatio-temporal screening conditions for TCCON sites and OCO-2 satellite Nadir mode observations

TCCON site	Local time	Observed location	Sample number	Reference
Tsukuba	12 : 48 – 12 : 58	36.05°N ± 0.5°, 140.12°E ± 0.5°	2078	Morino et al. (2022b)
Saga	13 : 30 – 13 : 40	33.24°N ± 0.5°, 130.29°E ± 0.5°	87	Shiomi et al. (2022)
Hefei	13 : 20 – 13 : 30	31.90°N ± 0.5°, 117.17°E ± 0.5°	984	Liu et al. (2022)
Xianghe	13 : 15 – 13 : 25	39.80°N ± 0.2°, 116.96°E ± 0.2°	2770	Zhou et al. (2022)
Rikubetsu	13 : 20 – 13 : 30	43.46°N ± 0.2°, 143.77°E ± 0.2°	723	Morino et al. (2022a)

Figure 14-1 presents time series comparisons of XCO<sub>2</sub> retrievals from the different TCCON sites, MLP-XCO<sub>2</sub> model, and  
 400 OCO-2 Nadir observations. Figure 14-2 displays the box plots of the differences between the MLP-XCO<sub>2</sub> model results, OCO-2 products, and TCCON site data. The plots at each of the five TCCON sites demonstrate the simulated data-trained MLP-XCO<sub>2</sub> model accurately predicts XCO<sub>2</sub> from the OCO-2 spectra. The model successfully captures seasonal variations and the

long-term XCO<sub>2</sub> growth trend over the 4-year study period. The reliable performance over time and across multiple TCCON sites further validates the model has learned generalizable representations of carbon cycle processes rather than overfitting to specifics of the simulated training data. By using realistic future simulations for training, the model provides robust and unbiased XCO<sub>2</sub> retrievals across a range of atmospheric conditions.

#### 5.4 Retrieval efficiency

In this study, the ReFRACtor forward model required 12.16 seconds per simulation case (two absorption bands) using an AMD Ryzen-7 5800X computer. The OCO-2 retrieval based on Bayesian optimization typically needs over three iterations to converge, indicating at least 36.48 seconds per retrieval. In contrast, the MLP-XCO<sub>2</sub> model demonstrated remarkable efficiency on the same hardware. It required just 1.14 seconds total to retrieve XCO<sub>2</sub> from 6642 OCO-2 test spectra across all five TCCON sites, averaging 0.17 milliseconds per sample with GPU RTX 3080Ti. This rapid inversion drastically reduces processing times compared to traditional methods. While machine learning models need significant upfront time for training data generation and hyperparameter tuning, the prediction is extremely fast once deployed. This enables near real-time processing ideal for operational satellite data streams. Furthermore, the precision and efficiency of neural networks make them well-suited to meet future demands of high-resolution global greenhouse gas monitoring, enabling millisecond-scale XCO<sub>2</sub> retrievals suitable for large-scale satellite analysis.

## 6 Conclusions

This proof-of-concept study aims to use the efficient regression inversion capability of the machine learning method to develop machine learning models based on simulated atmospheric radiative transfer data for efficient inversion of satellite observed spectra to retrieve XCO<sub>2</sub>. This helps overcome the low efficiency in traditional optimization-based iterative algorithms for XCO<sub>2</sub> retrievals. In the presented study, XCO<sub>2</sub> inversion models using both satellite product based and simulation based data were developed, trained and tested. Long-time series inversion and prediction of OCO-2 observations over East Asia were also performed using the developed models. The results were compared with OCO-2 and TCCON retrievals, showing the simulation data based machine learning models can effectively eliminate lagging biases while achieving millisecond-level (<1 ms) inversion efficiency, good accuracy (**less than 1.8 ppm**), local emission source capture, and long-term prediction stability. **It should be noted that our current MLP-XCO<sub>2</sub> model does not provide direct uncertainty estimates, estimating prediction intervals is an important next step for future improvements. Additionally, to provide good prior information while preventing the model from potentially focusing solely on interpolation rather than learning about actual CO<sub>2</sub> increases within spectra, our investigation has suggested that integrating additional contextual information, such as the "year," can offer valuable context for XCO<sub>2</sub> retrieval. However, the underlying mechanisms behind this improvement may require further investigation.**

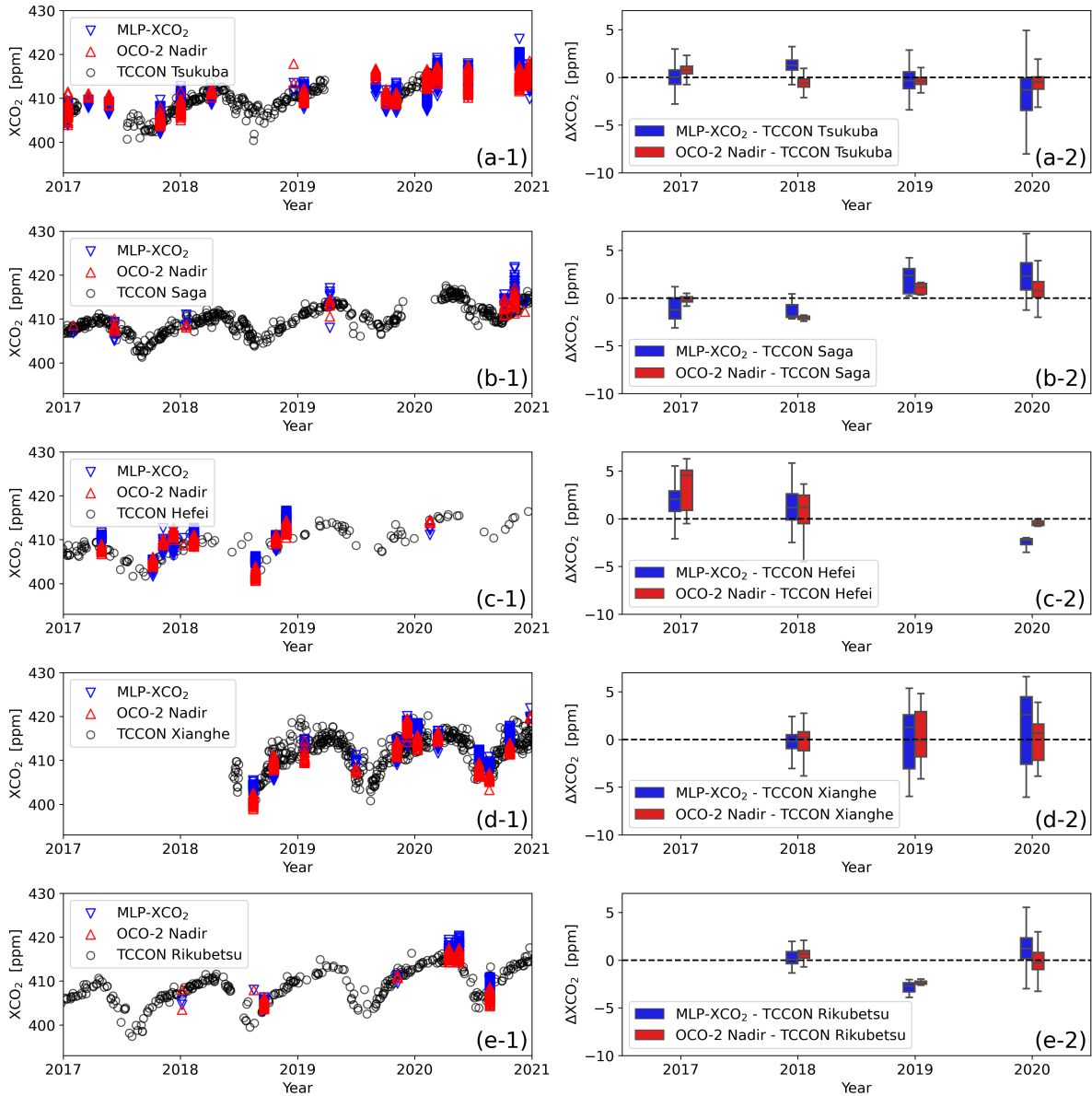


**Figure 14.** Comparisons of  $XCO_2$  results from 2017 to 2020 across five TCCON sites. Panel (a-1)-(e-1) show the time series comparisons of  $XCO_2$  retrievals from the different TCCON sites, MLP- $XCO_2$  model, and OCO-2 L2Lite Nadir observations for the Tsukuba, Saga, Hefei, Xianghe and Rikubetsu site, respectively, with data screening conditions as defined in Table 4. Panel (a-2)-(e-2) present the boxplots depicting the differences ( $\Delta XCO_2$ ) between the MLP- $XCO_2$  model and OCO-2 products in comparison to the TCCON results for each year. The boxes showing the middle half of the data, from the 25% to the 75% percentiles. The median (50%) is represented by the line within each box. The whiskers encompass the central 90% of the data, extending from the 5% to the 95% percentiles.

*Code availability.* The ReFRACtor model and its OCO retrieval implementation can be accessed from the Github ReFRACtor repository (<https://github.com/ReFRACtor>, last accessed in August 2023). The codes and models used in this study have been uploaded to GitHub and can be accessed at: [https://github.com/TaoRen-Rad/XCO2\\_retrieval](https://github.com/TaoRen-Rad/XCO2_retrieval). For access to the dataset, please send requests to Tao  
435 Ren (tao.ren@sjtu.edu.cn).

*Data availability.* The OCO-2 products (including OCO-2 L1B, Met, L2std and L2Lite files) are available from Goddard Earth Sciences Data and Information Services Center (<https://disc.gsfc.nasa.gov/datasets/>, last access: March 2023). The TCCON site products are available from TCCON DATA ACHIEVE (<https://tccodata.org/>, last access: March 2023).

*Financial support.* This research has been supported by the National Natural Science Foundation of China (Grants Nos. 52276077 and  
440 52120105009)

*Author contributions.* FX and TR designed the study. FX made updates and modifications for the Refractor forward model and developed the machine learning code, carried out the tests and result analysis under the supervision of TR. FX and TR prepared the manuscript. All authors reviewed the manuscript.

*Competing interests.* The corresponding author has declared that none of the authors has any competing interests.

445 *Disclaimer.* Publisher's note: Copernicus Publications remains neutral with regard to jurisdictional claims in published maps and institutional affiliations.

*Acknowledgements.* We gratefully acknowledge the TCCON Data Archive hosted by CaltechDATA at <https://tccodata.org> for providing the TCCON data for our study. Our thanks also go to the OCO-2 Science Team for the OCO-2 project. We appreciate our colleagues for their feedback and our affiliated institutions for their unwavering support.



## 450 References

- Bacour, C., Bréon, F.-M., and Chevallier, F.: On the challenge posed by the estimation of XCO<sub>2</sub> from OCO-2 observations in near-real time based on artificial neural network, *IWGGMS-19*, 2023.
- Braverman, A., Cressie, N., Kang, E., Katzfuss, M., Ma, P., Michalak, A., Nguyen, H., Stough, T., and Yadav, V.: Fusion of AIRS and OCO-2 carbon dioxide data for mapping lower-atmospheric CO<sub>2</sub>, 2015.
- 455 Bréon, F.-M., David, L., Chatelanaz, P., and Chevallier, F.: On the potential of a neural-network-based approach for estimating XCO<sub>2</sub> from OCO-2 measurements, *Atmospheric Measurement Techniques*, 15, 5219–5234, <https://doi.org/10.5194/amt-15-5219-2022>, 2022.
- Cansot, E., Pistre, L., Castelnau, M., Landiech, P., Georges, L., Gaeremynck, Y., and Bernard, P.: MicroCarb instrument, overview and first results, in: *International Conference on Space Optics — ICSO 2022*, edited by Minoglou, K., Karafolas, N., and Cugny, B., vol. 12777, p. 1277734, *International Society for Optics and Photonics, SPIE*, <https://doi.org/10.1117/12.2690330>, 2023.
- 460 Carvalho, A. R., Ramos, F. M., and Carvalho, J. C.: Retrieval of carbon dioxide vertical concentration profiles from satellite data using artificial neural networks, *Trends in Computational and Applied Mathematics*, 11, 205–216, <https://doi.org/10.5540/tema.2010.011.03.0205>, 2010.
- Chen, T. and Guestrin, C.: Xgboost: A scalable tree boosting system, in: *Proceedings of the 22nd acm sigkdd international conference on knowledge discovery and data mining*, pp. 785–794, 2016.
- 465 Cogan, A., Boesch, H., Parker, R., Feng, L., Palmer, P., Blavier, J.-F., Deutscher, N. M., Macatangay, R., Notholt, J., Roehl, C., et al.: Atmospheric carbon dioxide retrieved from the Greenhouse gases Observing SATellite (GOSAT): comparison with ground-based TCCON observations and GEOS-Chem model calculations, *Journal of Geophysical Research: Atmospheres*, 117, <https://doi.org/10.1029/2012JD018087>, 2012.
- Crisp, D., Fisher, B., O’Dell, C., Frankenberg, C., Basilio, R., Bösch, H., Brown, L., Castano, R., Connor, B., Deutscher, N., et al.: 470 The ACOS CO<sub>2</sub> retrieval algorithm—part II: global XCO<sub>2</sub> data characterization, *Atmospheric Measurement Techniques*, 5, 687–707, <https://doi.org/10.5194/amt-5-687-2012>, 2012.
- Crisp, D., Pollock, H. R., Rosenberg, R., Chapsky, L., Lee, R. A., Oyafuso, F. A., Frankenberg, C., O’Dell, C. W., Bruegge, C. J., Doran, G. B., et al.: The on-orbit performance of the Orbiting Carbon Observatory-2 (OCO-2) instrument and its radiometrically calibrated products, *Atmospheric Measurement Techniques*, 10, 59–81, <https://doi.org/10.5194/amt-10-59-2017>, 2017.
- 475 Crisp, D., O’Dell, C., Eldering, A., Fisher, B., et al.: Orbiting carbon observatory (OCO) - 2 level 2 full physics algorithm theoretical basis document Version 3.0 – Rev 1, [https://docserver.gesdisc.eosdis.nasa.gov/public/project/OCO/OCO\\_L2\\_ATBD.pdf](https://docserver.gesdisc.eosdis.nasa.gov/public/project/OCO/OCO_L2_ATBD.pdf), 2021.
- David, L., Bréon, F.-M., and Chevallier, F.: XCO<sub>2</sub> estimates from the OCO-2 measurements using a neural network approach, *Atmospheric Measurement Techniques*, 14, 117–132, <https://doi.org/10.5194/amt-14-117-2021>, 2021.
- Eldering, A., Taylor, T. E., O’Dell, C. W., and Pavlick, R.: The OCO-3 mission: measurement objectives and expected performance based on 480 1 year of simulated data, *Atmospheric Measurement Techniques*, 12, 2341–2370, <https://doi.org/10.5194/amt-12-2341-2019>, 2019.
- Gribanov, K., Imasu, R., and Zakharov, V.: Neural networks for CO<sub>2</sub> profile retrieval from the data of GOSAT/TANSO-FTS, *Atmospheric and Oceanic Optics*, 23, 42–47, <https://doi.org/10.1134/S1024856010010094>, 2010.
- Hamazaki, T., Kaneko, Y., Kuze, A., and Kondo, K.: Fourier transform spectrometer for greenhouse gases observing satellite (GOSAT), in: *Enabling sensor and platform technologies for spaceborne remote sensing*, vol. 5659, pp. 73–80, *SPIE*, <https://doi.org/10.1117/12.581198>, 485 2005.

- Imasu, R., Matsunaga, T., Nakajima, M., Yoshida, Y., Shiomi, K., Morino, I., Saitoh, N., Niwa, Y., Someya, Y., Oishi, Y., et al.: Greenhouse gases Observing SATellite 2 (GOSAT-2): mission overview, *Progress in Earth and Planetary Science*, 10, 33, <https://doi.org/10.1186/s40645-023-00562-2>, 2023.
- 490 Iwasaki, C., Imasu, R., Bril, A., Oshchepkov, S., Yoshida, Y., Yokota, T., Zakharov, V., Griбанov, K., and Rokotyan, N.: Optimization of the Photon Path Length Probability Density Function-Simultaneous (PPDF-S) Method and Evaluation of CO<sub>2</sub> Retrieval Performance Under Dense Aerosol Conditions, *Sensors*, 19, 1262, 2019.
- Jin, Z., Tian, X., Han, R., Fu, Y., Li, X., Mao, H., Chen, C., and GAO, J.: Tan-Tracker global daily NEE and ocean carbon fluxes for 2015-2019 (TT2021 dataset), <https://doi.org/10.11888/Meteoro.tpsc.271317>, 2021.
- Keely, W. R., Mauceri, S., Crowell, S., and O'Dell, C. W.: A nonlinear data-driven approach to bias correction of XCO<sub>2</sub> for NASA's OCO-2  
495 ACOS version 10, *Atmospheric Measurement Techniques*, 16, 5725–5748, 2023.
- Kuze, A., Suto, H., Nakajima, M., and Hamazaki, T.: Thermal and near infrared sensor for carbon observation Fourier-transform spectrometer on the Greenhouse Gases Observing Satellite for greenhouse gases monitoring, *Applied optics*, 48, 6716–6733, <https://doi.org/10.1364/AO.48.006716>, 2009.
- Li, Y., Jiang, F., Jia, M., Feng, S., Lai, Y., Ding, J., He, W., Wang, H., Wu, M., Wang, J., et al.: Improved estimation of CO<sub>2</sub> emissions from  
500 thermal power plants based on OCO-2 XCO<sub>2</sub> retrieval using inline plume simulation, *Science of The Total Environment*, p. 169586, 2023.
- Liang, A., Gong, W., Han, G., and Xiang, C.: Comparison of satellite-observed XCO<sub>2</sub> from GOSAT, OCO-2, and ground-based TCCON, *Remote Sensing*, 9, 1033, <https://doi.org/10.3390/rs9101033>, 2017.
- Liu, C., Wang, W., Sun, Y., and Shan, C.: TCCON data from Hefei, China, Release GGG2020R0. TCCON data archive, hosted by Caltech-DATA, California Institute of Technology, Pasadena, CA, U.S.A., <https://doi.org/10.14291/tcon.ggg2020.hefei01.R0>, 2022.
- 505 Liu, Y., Wang, J., Yao, L., Chen, X., Cai, Z., Yang, D., Yin, Z., Gu, S., Tian, L., Lu, N., et al.: The TanSat mission: preliminary global observations, *Science Bulletin*, 63, 1200–1207, <https://doi.org/10.1016/j.scib.2018.08.004>, 2018.
- Marchetti, Y., Rosenberg, R., and Crisp, D.: Classification of anomalous pixels in the focal plane arrays of Orbiting Carbon Observatory-2 and-3 via machine learning, *Remote Sensing*, 11, 2901, <https://doi.org/10.3390/rs11242901>, 2019.
- Matsunaga, T. and Tanimoto, H.: Greenhouse gas observation by TANSO-3 onboard GOSAT-GW, in: *Sensors, Systems, and Next-Generation Satellites XXVI*, vol. 12264, pp. 86–90, SPIE, <https://doi.org/10.1117/12.2639221>, 2022.
- 510 McDuffie, J., Bowman, K. W., Hobbs, J., Natraj, V., Val, S., Sarkissian, E., and Thill, M. D.: ReFRACtor: Reusable Software Framework for Retrieval of Satellite Atmospheric Composition, in: *AGU Fall Meeting Abstracts*, vol. 2018, pp. A11F–2282, 2018.
- Meng, G., Wen, Y., Zhang, M., Gu, Y., Xiong, W., Wang, Z., and Niu, S.: The status and development proposal of carbon sources and sinks monitoring satellite system, *Carbon Neutrality*, 1, 32, 2022.
- 515 Messerschmidt, J., Geibel, M., Blumenstock, T., Chen, H., Deutscher, N., Engel, A., Feist, D. G., Gerbig, C., Gisi, M., Hase, F., et al.: Calibration of TCCON column-averaged CO<sub>2</sub>: the first aircraft campaign over European TCCON sites, *Atmospheric Chemistry and Physics*, 11, 10765–10777, <https://doi.org/10.5194/acp-11-10765-2011>, 2011.
- Modest, M. F. and Mazumder, S.: *Radiative heat transfer*, Academic press, 2021.
- Morino, I., Ohyama, H., Hori, A., and Ikegami, H.: TCCON data from Rikubetsu, Hokkaido, Japan, Release  
520 GGG2020R0. TCCON data archive, hosted by CaltechDATA, California Institute of Technology, Pasadena, CA, U.S.A., <https://doi.org/10.14291/tcon.ggg2020.rikubetsu01.R0>, 2022a.

- Morino, I., Ohyama, H., Hori, A., and Ikegami, H.: TCCON data from Tsukuba, Ibaraki, Japan, 125HR, Release GGG2020R0. TCCON data archive, hosted by CaltechDATA, California Institute of Technology, Pasadena, CA, U.S.A., <https://doi.org/10.14291/tcon.ggg2020.tsukuba02.R0>, 2022b.
- 525 Natraj, V. and Spurr, R. J.: A fast linearized pseudo-spherical two orders of scattering model to account for polarization in vertically inhomogeneous scattering-absorbing media, *Journal of Quantitative Spectroscopy and Radiative Transfer*, 107, 263–293, <https://doi.org/10.1016/j.jqsrt.2007.02.011>, 2007.
- OCO-2 Science Team, Gunson, M., and Eldering, A.: OCO-2 Level 1B calibrated, geolocated science spectra, Retrospective Processing V10r, Greenbelt, MD, USA, Goddard Earth Sciences Data and Information Services Center (GES DISC),  
530 <https://doi.org/10.5067/6O3GEUK7U2JG>, accessed: [August 2023], 2019.
- OCO-2 Science Team, Gunson, M., and Eldering, A.: OCO-2 Level 2 bias-corrected XCO<sub>2</sub> and other select fields from the full-physics retrieval aggregated as daily files, Retrospective processing V10r, Greenbelt, MD, USA, Goddard Earth Sciences Data and Information Services Center (GES DISC), <https://doi.org/10.5067/6SBROTA57TFH>, accessed: [August 2023], 2020a.
- OCO-2 Science Team, Gunson, M., and Eldering, A.: OCO-2 Level 2 geolocated XCO<sub>2</sub> retrievals results, physical model, Retrospective Processing V10r, Greenbelt, MD, USA, Goddard Earth Sciences Data and Information Services Center (GES DISC),  
535 <https://doi.org/10.5067/E4E140XDMPO2>, accessed: [August 2023], 2020b.
- O’Dell, C., Connor, B., Bösch, H., O’Brien, D., Frankenberg, C., Castano, R., Christi, M., Eldering, D., Fisher, B., Gunson, M., et al.: The ACOS CO<sub>2</sub> retrieval algorithm—Part 1: Description and validation against synthetic observations, *Atmospheric Measurement Techniques*, 5, 99–121, <https://doi.org/10.5194/amt-5-99-2012>, 2012.
- 540 Payne, V. H., Drouin, B. J., Oyafuso, F., Kuai, L., Fisher, B. M., Sung, K., Nemchick, D., Crawford, T. J., Smyth, M., Crisp, D., et al.: Absorption coefficient (ABSCO) tables for the Orbiting Carbon Observatories: version 5.1, *Journal of Quantitative Spectroscopy and Radiative Transfer*, 255, 107 217, <https://doi.org/10.1016/j.jqsrt.2020.107217>, 2020.
- Rodgers, C. D.: *Inverse methods for atmospheric sounding: theory and practice*, vol. 2, World scientific, 2000.
- Shiomi, K., Kawakami, S., Ohyama, H., Arai, K., Okumura, H., Ikegami, H., and Usami, M.: TCCON data from Saga, Japan,  
545 Release GGG2020R0. TCCON data archive, hosted by CaltechDATA, California Institute of Technology, Pasadena, CA, U.S.A., <https://doi.org/10.14291/tcon.ggg2020.saga01.R0>, 2022.
- Sierk, B., Fernandez, V., Bézy, J.-L., Meijer, Y., Durand, Y., Courrèges-Lacoste, G. B., Pachot, C., Löscher, A., Nett, H., Minoglou, K., et al.: The Copernicus CO<sub>2</sub>M mission for monitoring anthropogenic carbon dioxide emissions from space, in: *International Conference on Space Optics—ICSO 2020*, vol. 11852, pp. 1563–1580, SPIE, <https://doi.org/10.1117/12.2599613>, 2021.
- 550 Spurr, R.: LIDORT and VLIDORT: Linearized pseudo-spherical scalar and vector discrete ordinate radiative transfer models for use in remote sensing retrieval problems, *Light scattering reviews 3: Light scattering and reflection*, pp. 229–275, [https://doi.org/10.1007/978-3-540-48546-9\\_7](https://doi.org/10.1007/978-3-540-48546-9_7), 2008.
- Wunch, D., Toon, G. C., Blavier, J.-F. L., Washenfelder, R. A., Notholt, J., Connor, B. J., Griffith, D. W. T., Sherlock, V., and Wennberg, P. O.: The Total Carbon Column Observing Network, *Philos. Trans. R. Soc. A Math. Phys. Eng. Sci.*, 369(1943), 2087–2112,  
555 <https://doi.org/10.1098/rsta.2010.0240>, 2011.
- Wunch, D., Toon, G. C., Sherlock, V., Deutscher, N. M., Liu, C., Feist, D. G., and Wennberg, P. O.: The Total Carbon Column Observing Network’s GGG2014 Data Version, Pasadena, California, <https://doi.org/10.14291/TCCON.GGG2014.DOCUMENTATION.R0/1221662>, 2015.

- Wunch, D., Wennberg, P. O., Osterman, G., Fisher, B., Naylor, B., Roehl, C. M., O'Dell, C., Mandrake, L., Viatte, C., Kiel, M., et al.:  
560 Comparisons of the orbiting carbon observatory-2 (OCO-2) XCO<sub>2</sub> measurements with TCCON, *Atmospheric Measurement Techniques*,  
10, 2209–2238, <https://doi.org/10.5194/amt-10-2209-2017>, 2017.
- Yoshida, Y., Kikuchi, N., Morino, I., Uchino, O., Oshchepkov, S., Bril, A., Saeki, T., Schutgens, N., Toon, G., Wunch, D., et al.: Improvement  
of the retrieval algorithm for GOSAT SWIR XCO<sub>2</sub> and XCH<sub>4</sub> and their validation using TCCON data, *Atmospheric Measurement  
Techniques*, 6, 1533–1547, <https://doi.org/10.5194/amt-6-1533-2013>, 2013.
- 565 Zehr, S.: The sociology of global climate change, *Wiley Interdisciplinary Reviews: Climate Change*, 6, 129–150,  
<https://doi.org/10.1002/wcc.328>, 2015.
- Zhao, Z., Xie, F., Ren, T., and Zhao, C.: Atmospheric CO<sub>2</sub> retrieval from satellite spectral measurements by a two-step machine learning  
approach, *Journal of Quantitative Spectroscopy and Radiative Transfer*, 278, 108 006, <https://doi.org/10.1016/j.jqsrt.2021.108006>, 2022.
- Zhou, M., Wang, P., Nan, W., Yang, Y., Kumps, N., Hermans, C., and De Mazière, M.: TCCON data from Xianghe,  
570 <https://doi.org/10.14291/tcon.ggg2020.xianghe01.R0>, 2022.